Insights into magnetoelectric coupling mechanism of the room-temperature multiferroic Sr3Co2Fe24041 from domain observation

doi: 10.1103/PhysRevB.100.094444

Insights into magnetoelectric coupling mechanism of the room-temperature multiferroic $Sr_3Co_2Fe_{24}O_{41}$ from domain observation

Hiroki Ueda,[1,*,†] Yoshikazu Tanaka,[2] Yusuke Wakabayashi,[1,‡] and Tsuyoshi Kimura[3]

[1]*Division of Materials Physics, Graduate School of Engineering Science, Osaka University, Toyonaka, Osaka 560-8531, Japan*

[2]*RIKEN SPring-8 Center, Sayo, Hyogo 679-5148, Japan*

[3]*Department of Advanced Materials Science, University of Tokyo, Kashiwa, Chiba 277-8561, Japan*

(Received 18 June 2019; published 27 September 2019)

The mechanism of a magnetoelectric coupling in a room-temperature multiferroic, $Sr_3Co_2Fe_{24}O_{41}$, with the Z-type hexaferrite structure, is examined by three approaches: observations of domain structures and their field responses, measurements of magnetic-field effect on electric polarization, i.e., magnetoelectric effect, and phenomenological discussions on the interplay among coexisting order parameters. With use of a resonant soft x-ray microdiffraction technique, we visualized magnetic-field responses of two types of magnetic domains ascribed to ferrimagnetic and spiral components inherent in a transverse conical magnetic structure of the hexaferrite. A simultaneous inversion of these magnetic domains by a magnetic-field reversal was observed, meaning that the process of a magnetization reversal corresponds to a 180° rotation of the cone axis. The reversal process of the magnetic structure, together with experimental results of the magnetoelectric effect, leads us to the conclusion that the magnetoelectricity in the Z-type hexaferrite originates mainly from the spin-dependent metal-ligand orbital hybridization, with minor contribution from the asymmetric spin-exchange interaction. Furthermore, such a mechanism is discussed by the symmetry analysis based on the Landau theory and is well described in terms of couplings among the coexisting order parameters included in the free energy. Thus, observations on field responses of multiple domains in multiferroics provide insights into underlying microscopic magnetoelectric coupling mechanisms.

DOI: 10.1103/PhysRevB.100.094444

I. INTRODUCTION

Spontaneous symmetry breaking in condensed-matter physics is ascribed to the evolution of an order parameter. A set of distinct order parameters is provided by the symmetry of a matter and separates the matter into domains characterized by the sign and/or orientation of the parameters. The manipulation of domains by an external field is the key principle to exploit ferroic materials such as ferroelectrics and ferromagnets. In multiferroics exhibiting both ferroelectricity and (anti)ferromagnetism [1,2], at least two types of order parameters, e.g., electric polarization P and magnetization M, coexist. One of the most fascinating characteristics in multiferroics is the interplay among the coexisting order parameters, which leads to remarkable magnetoelectric (ME) responses to external fields. For example, it was reported that a reversal of M accompanies that of P in multiferroics where ferromagnetism and ferroelectricity originate from a transverse conical (TC) spin order breaking time-reversal and space-inversion symmetries simultaneously [3,4]. In such multiferroics, it was pointed out that their ME responses are critically affected by domain-wall couplings such as a clamping of domain walls ascribed to different order parameters [3,5]. In fact, the ME response in a conical magnet, Mn_2GeO_4, has been explained in terms of not only coupled order parameters but also their domain responses through direct observations of the change in domain population as well as domain pattern by applying external magnetic and/or electric fields [6,7].

In Mn_2GeO_4, a reversal of M inverts the sign of P in each ferroelectric domain without any change of the ferroelectric domain pattern [7]. This inversion process shows that ferroelectric domain walls are clamped with ferromagnetic ones. By means of a phenomenological approach based on the Landau theory, when the symmetry allows the interplay among multiple order parameters coexisting in the material, one finds that it plays an essential role for such a domain inversion as well as the emergence of the ME effect, i.e., magnetic control of P [6,8]. Therefore, such interplay among order parameters can give rise to a promising basic concept for the nontrivial control and understanding of properties inherent in materials which show multiple electronic and/or structural orders, such as multiferroics.

Among a variety of multiferroics, iron-based oxides with hexagonal crystal structures, termed hexaferrites, have been attracting considerable attention. This is because they are rare single-phase multiferroics that allow high-temperature and low-magnetic-field operation with remarkable ME responses, either magnetic-field-induced ferroelectricity or electric-field-induced magnetism [9,10]. To date, ME effects have been observed in several types of hexaferrites such as Y-type $(Ba, Sr)_2Me_2Fe_{12}O_{22}$ [11–14],

*Present address: Swiss Light Source, Paul Scherrer Institut, 5232 Villigen, Switzerland.

†hiroki.ueda@psi.ch

‡Present address: Department of Physics, Tohoku University, Sendai, Miyagi 980-8578, Japan.

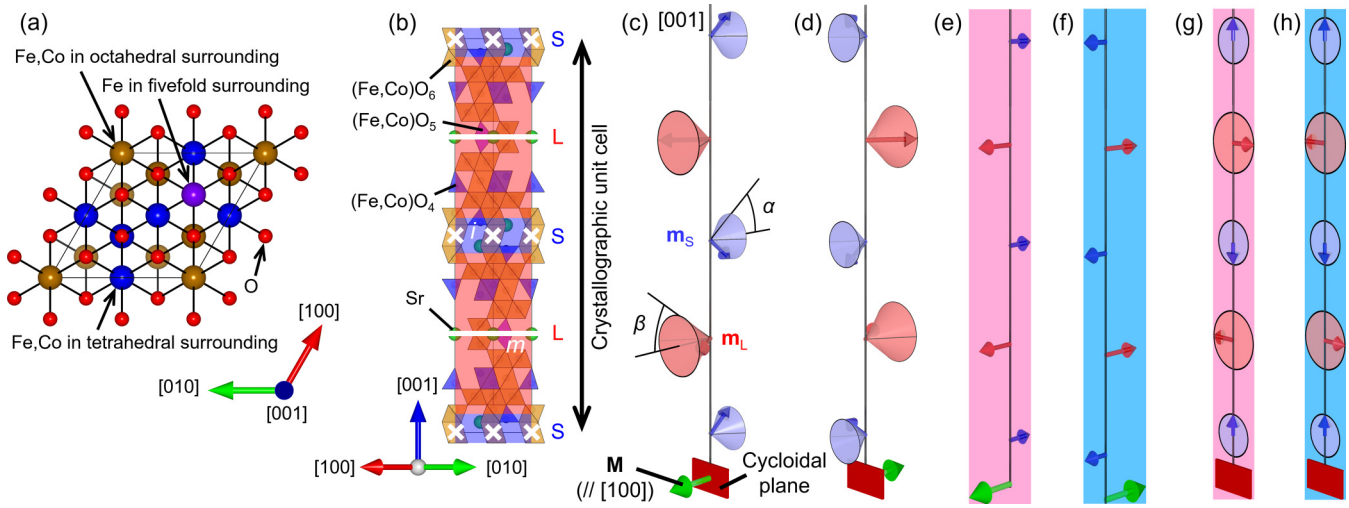

FIG. 1. (a), (b) Crystal structure of $Sr_3Co_2Fe_{24}O_{41}$ viewed along [001] (a) and [110] (b). White crosses and horizontal lines in (b) represent inversion centers and mirror planes, respectively. (c, d) The transverse conical (TC) magnetic structure proposed for $Sr_3Co_2Fe_{24}O_{41}$ [19]. The red (blue) arrows represent net magnetic moments in the respective L (S) blocks. The brown planes and the green arrows show the cycloidal plane and net magnetization M in the whole unit cell, respectively. The TC structures formed in a domain (c) before and (d) after an M reversal where both M and spin helicity are inverted by a 180° rotation of the cone axis around [001]. The TC structure drawn in (c) [(d)] can be regarded as the combination of a ferrimagnetic component (e) [(f)] and a cycloidal one (g) [(h)]. The states with pinkish (light-bluish) background [(e)-(h)] correspond to the red- (blue-) colored regions in Figs. 6(a) and 6(b) for the ferrimagnetic component [(e) and (f)] and those in Figs. 6(c) and 6(d) for the cycloidal one [(g) and (h)].

M-type $(Ba, Sr)(Fe, Sc, Mg)_{12}O_{19}$ [15], and Z-type $(Ba, Sr)_3Me_2Fe_{24}O_{41}$ [16,17], where Me is a divalent metal ion. It is considered that a characteristic common to these ME hexaferrites is a spontaneous (or magnetic-field-induced) development of a TC magnetic structure in which both M and P coexist [18,19]. The TC structure is composed of a cycloidal spin-spiral component and a collinear-ferrimagnetic component. The former induces P through the asymmetric spin-exchange interaction: the so-called spin-current [or the inverse Dzyaloshinskii-Moriya (DM)] interaction [20–22]. This interaction had long been believed as a main origin of ME coupling in the hexaferrite family.

Recently, however, it was proposed that the ME-coupling mechanism depends on types of hexaferrites on the basis of experimental observations of their ME effects and consideration of the symmetries in their structures [23,24]. According to these studies, the ME coupling in the Y-type hexaferrite [23] is ascribed to the asymmetric spin-exchange interaction, as expected in most of the previous studies, while that in the Z-type hexaferrite [23,24] is mainly ascribed to the spin-dependent metal-ligand orbital hybridization [25]. However, due to the complex crystallographic and magnetic structures of ME hexaferrites, their ME mechanisms were discussed only on the basis of their macroscopic properties such as M and P, as well as the modulation wave vectors $\mathbf{k}$ of their magnetic structures.

The purpose of this study is to provide insights into the ME-coupling mechanism in a room-temperature multiferroic Z-type hexaferrite, $Sr_3Co_2Fe_{24}O_{41}$, showing a TC magnetic structure [16,17,19] from the viewpoint of microscopic magnetic domains rather than its macroscopic ME properties. We examine magnetic-field responses of two types of magnetic domains formed by the evolution of coexisting order parameters inherent in the TC magnetic structure by adopting a resonant soft x-ray microdiffraction technique using circularly polarized incident x rays. This technique allows us to separately observe domain structures ascribed to the coexisting order parameters. Judging from the magnetic-field response of the magnetic domains, i.e., microscopic spatial distribution of order parameters, together with that of P, i.e., macroscopic order parameters, the ME coupling in the Z-type hexaferrite is dominantly ascribed to the spin-dependent metal-ligand orbital hybridization mechanism. In addition, we verify the ME-coupling mechanism in the Z-type hexaferrite with the complex crystallographic and magnetic structures through a symmetry-based discussion of the interplay among the coexisting order parameters.

II. SAMPLE AND EXPERIMENT

The Z-type hexaferrite $Sr_3Co_2Fe_{24}O_{41}$ belongs to the hexagonal space group $P6_3/mmc$ with lattice parameters $a \approx 5.87$ Å and $c \approx 52.07$ Å [16,26]. Figures 1(a) and 1(b) display its crystal structure viewed along [001] and [110], respectively. The complex crystal structure is divided into small (S) and large (L) magnetic blocks stacked along the [001] direction alternately. The effective moments in the S and L blocks are estimated to be 5.9 μ_B and 39.8 μ_B, respectively, where μ_B is the Bohr magneton. In this estimation, the occupancies of Fe^{3+} and Co^{2+} for the respective magnetic sites are taken into account [27]. Note that the L block of the Z-type structure has a mirror plane normal to [001] at the center of the block [white lines in Fig. 1(b)]. The magnetic structure of $Sr_3Co_2Fe_{24}O_{41}$ at room temperature in the absence of a magnetic field B was reported to be the TC structure [19], which is illustrated in Fig. 1(c). The net magnetization is parallel to the basal plane. This structure can be divided into a collinear-ferrimagnetic component with $\mathbf{k} = (0, 0, 0)$ [Fig. 1(e)] and a cycloidal

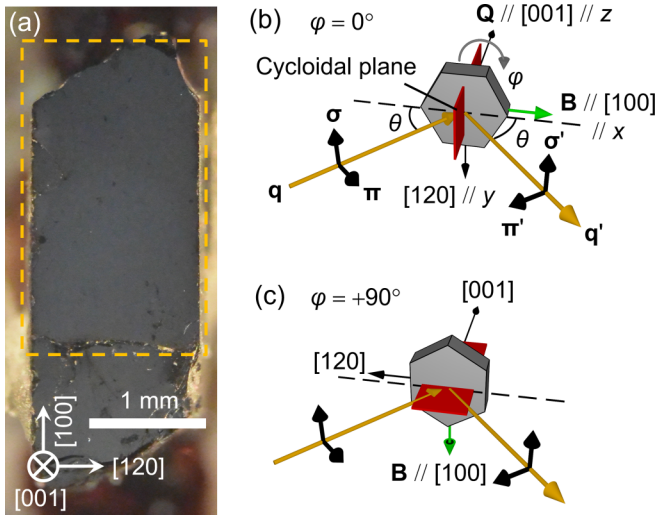

FIG. 2. (a) A photograph of the specimen. An orange dashed box roughly corresponds to the region where the intensity maps were obtained. (b), (c) Scattering geometries for the RXD measurements at (b) $\varphi = 0^\circ$ and (c) $+90^\circ$.

spin-spiral component with $\mathbf{k} = (0, 0, 1)$ [Fig. 1(g)]. Hereafter, we refer to the plane normal to macroscopic M in the TC structure as a cycloidal plane. We define the handedness of the cycloidal component such that magnetic moments in the right- (left-) handed domain are rotated counterclockwise (clockwise) from the lower to upper sides of the crystal structure [shown in Fig. 1(b)] viewed along [100] from the origin. To represent the handedness of the cycloidal component, we introduce vector spin chirality $\mathbf{C}$. The cross product of two magnetic moments at sites i and j, $\mathbf{m}_i$ and $\mathbf{m}_j$, respectively, defines $\mathbf{C}$ so that $\mathbf{C}$ between the sites, $\mathbf{C}_{ij}$, is described as

$$\mathbf{C}_{ij} = \mathbf{m}_i \times \mathbf{m}_j. \tag{1}$$

A cycloidal configuration of magnetic moments gives a uniform sign of $\mathbf{C}$ among any pairs of neighboring magnetic moments. The sign corresponds to the handedness of the component in right- and left-handed cycloidal spin-spiral domains shown in Figs. 1(g) and 1(h), respectively.

Single crystals of $Sr_3Co_2Fe_{24}O_{41}$ were grown by the Na_2O-Fe_2O_3 flux method similar to that described in Ref. [17]. Resonant x-ray diffraction (RXD) measurements on one of the crystals with a flat and clean cleaved face parallel to the (001) plane [see Fig. 2(a)] were performed at the beamline 17SU, SPring-8. Highly focused, circularly polarized, soft x rays whose beam size and photon energy $E_{\rm ph}$ were approximately $30 \times 15\,\mu{\rm m}^2$ and in the vicinity of the Fe L_3 edge ($\approx$710 eV), respectively, were utilized [28,29]. Here the degree of circular polarization for the incident beam is represented by the so-called Stokes parameter P_2 such that a beam with $P_2 = +1(-1)$ corresponds to the right- (left-) circularly polarized state [30]. The crystal was mounted with the [001] direction along the scattering vector $\mathbf{Q}$ ($= \mathbf{q} - \mathbf{q}'$, where $\mathbf{q}$ and $\mathbf{q}'$ are the wave vectors of the incident and diffracted x rays, respectively). All the RXD data shown in this paper were taken at room temperature and in B ($|B| \approx$ 0.3 T) along [100]. In this condition, the direction of M for the TC structure [31] is fixed along [100]. B was applied by using a pair of neodymium magnets. Two representative scattering geometries used in this RXD study are illustrated in Figs. 2(b) and 2(c), in which φ ($= 0^\circ$ or $+90^\circ$) is the azimuthal angle and θ is the Bragg angle. We define $\varphi = 0^\circ$ as the geometry where the [100] direction is parallel to the scattering plane [Fig. 2(b)]. The positive rotation of φ is defined as a counterclockwise direction along $\mathbf{Q}$. To observe the spatial distribution of magnetic domains, two-dimensional scans of the focused x-ray beam on the cleaved face were carried out.

Resonant scattering amplitude from a crystal through dipole transition is represented as

$$f = -a(\boldsymbol{\varepsilon}' \cdot \boldsymbol{\varepsilon}) + b\mathbf{F}_m \cdot (\boldsymbol{\varepsilon}' \times \boldsymbol{\varepsilon}). \tag{2}$$

Here $\boldsymbol{\varepsilon}$ ($\boldsymbol{\varepsilon}'$) is the polarization unit vector of an incident (scattered) beam, and b [$= -3/(4\pi q)i(F^1_{-1} - F^1_{+1})$] is a coefficient of the magnetic scattering term, which is linear to a local magnetic moment in the resonant elastic scattering length. $F^1_{+1(-1)}$ is the resonant strength of the dipole transition with a change 1 in orbital quantum number and a change 1 (-1) in magnetic quantum number, and q is the magnitude of the wave vector of an incident photon. $\mathbf{F}_m$ and a are magnetic and crystal structure factors, respectively, defined as

$$\mathbf{F}_m = \sum_j \mathbf{m}_j \exp(2\pi i \mathbf{Q} \cdot \mathbf{R}_j) \tag{3}$$

and

$$a = -\sum_j \left[f_0 + \frac{3}{4\pi q}\left(F^1_{-1} + F^1_{+1}\right)\right] \exp(2\pi i \mathbf{Q} \cdot \mathbf{R}_j). \tag{4}$$

Here f_0 is the Thomson scattering amplitude, and $\mathbf{m}_j$ and $\mathbf{R}_j$ are the unit vector parallel to the local magnetic moment and the atomic position vector, respectively, of site j. An RXD signal from a general magnetic material can be circular dichroic through the pure magnetic scattering and/or the charge-magnetic interference effect represented as

$$\left(\frac{d\sigma}{d\Omega}\right)^{\rm pure}_{P_2} = P_2|b|^2 {\rm Im}\{[\mathbf{F}_m \cdot (\hat{\mathbf{q}}' \times \hat{\mathbf{q}})](\mathbf{F}_m{}^* \cdot \hat{\mathbf{q}}')\} \tag{5}$$

and

$$\left(\frac{d\sigma}{d\Omega}\right)^{\rm inter}_{P_2} = -P_2 {\rm Im}(a^* b \mathbf{F}_m) \cdot (\hat{\mathbf{q}} + \hat{\mathbf{q}}' \cos 2\theta), \tag{6}$$

respectively [32]. Here the hat denotes the unit vector along each vector. The circular polarization-dependent part in the scattering cross section $d\sigma/d\Omega_{P_2}$ is discussed by using the flipping ratio (FR). FR is defined as the normalized difference intensity between the data obtained with right circularly polarized (RCP) and left circularly polarized (LCP) x rays, $(I_{\rm RCP} - I_{\rm LCP})/(I_{\rm RCP} + I_{\rm LCP})$ ($\propto d\sigma/d\Omega_{P_2}$).

For ME measurements, some of the single crystals were oriented by using the Laue x-ray diffraction method and cut into thin plates with the widest faces perpendicular to [120] or [100]. Silver paste was painted on the widest faces of the plates and used as electrodes. The specimen was inserted in a commercial superconducting magnet [Quantum Design Physical Property Measurement System (PPMS)]. The following ME poling procedure was carried out to make a single ME domain state in advance of each measurement. An electric field

$E_{pol}(= \pm 1\,\mathrm{MV/m})$ was applied at the paraelectric collinear-ferrimagnetic phase ($B = -3$ T). Subsequently, B was swept into the ferroelectric TC phase ($B = -0.3$ T), and E_{pol} was removed. Then the ME current was measured by using an electrometer (Keithley 6517A) while sweeping B at a rate of $\sim$1.1 T/min. By integrating the ME current as a function of time, P was obtained as a function of B. In this study, we measured P normal to and parallel to B in the basal plane. All the ME measurements were carried out at 10 K, where the sample resistivity is high enough to measure intrinsic ME current.

III. RESULTS AND DISCUSSION

A. Resonant x-ray diffraction

Figure 3(a) shows the 00L profile obtained on a certain sample position by using an RCP x-ray beam at $E_{ph} = 709.2$ eV and $\varphi = +90^\circ$, where the cycloidal plane is parallel to the scattering plane [Fig. 2(c)]. In addition to the 002n Bragg reflections (n = integer), finite 002$n \pm 1$ space-group forbidden reflections exist. The result is well explained by the TC structure, because the cycloidal component with $\mathbf{k} = (0, 0, 1)$ causes magnetic satellites around the Bragg reflections [19]. As displayed in Figs. 3(b) and 3(c), the change of sign in the circularly polarized state of incident x rays [$P_2 = +1$ (RCP) or -1 (LCP)] yields substantially different intensities of both the space-group allowed and forbidden reflections, i.e., 004 and 003, except for 004 at $\varphi = +90^\circ$. Photon-energy profiles of the intensities at 004 and 003 are shown in Fig. 4 together with an x-ray absorption spectrum (XAS) obtained by the total electron yield method for comparison. All the intensities of the reflections are clearly enhanced in the vicinity of the Fe L_3 edge and become circular dichroic around the absorption edge, except for 004 at $\varphi = +90^\circ$. The circular dichroism of the reflections is found to be due to the resonant effect.

1. Circular dichroism caused by the ferromagnetic order parameter

We apply the TC structure of $Sr_3Co_2Fe_{24}O_{41}$ to Eq. (6) with use of the Cartesian coordinate shown in Fig. 2(b) to discuss what causes the circular dichroism of 004. The structure can be described by using the half opening angles of the conical structure, α and β, in an S block and an L block, respectively [see Fig. 1(c)]. The magnetic moments of the respective magnetic blocks are tabulated in Table I, where m_S and m_L are the magnetic moments of an S block and an L block, respectively.

Applying them to Eq. (3), one gets $\mathbf{F}_m$ at 004 as

$$\mathbf{F}_m^{004} = 2N[(m_L \cos\beta - m_S \cos\alpha)\cos\varphi, \\ (m_L \cos\beta - m_S \cos\alpha)\sin\varphi,\ 0]. \quad (7)$$

Here N is the unit cell contributing to the scattering. Note that the collinear-ferrimagnetic component with $\mathbf{k} = \mathbf{0}$ contributes to the 004 reflection, but the cycloidal spin-spiral one does not. The circular dichroism through the pure magnetic scattering term [Eq. (5)] is found to be zero because $\mathbf{F}_m^{004}$ possesses only real number components. By contrast, the interference term [Eq. (6)] provides a finite circular dichroic signal at 004 because both the charge and magnetic scatterings contribute to the 004 reflection in the TC structure, that is, a and $\mathbf{F}_m$ are finite at 004. By plugging Eq. (7) into Eq. (6), $d\sigma/d\Omega_{P_2}$ at 004 is obtained as

$$\left(\frac{d\sigma}{d\Omega}\right)_{P_2}^{004} = -4NP_2\mathrm{Im}(a_{004}{}^* b)(m_L \cos\beta \\ - m_S \cos\alpha)\cos\varphi \cos^3\theta. \quad (8)$$

Equation (8) indicates that the ferrimagnetic component, $m_L\cos\beta - m_S\cos\alpha \propto M$, in the TC structure gives rise to circular dichroism at 004 through the interference as reported in ferromagnets [33–35]. The absence of the circular dichroism in 004 at $\varphi = +90^\circ$ [upper panel of Fig. 3(c)] well supports

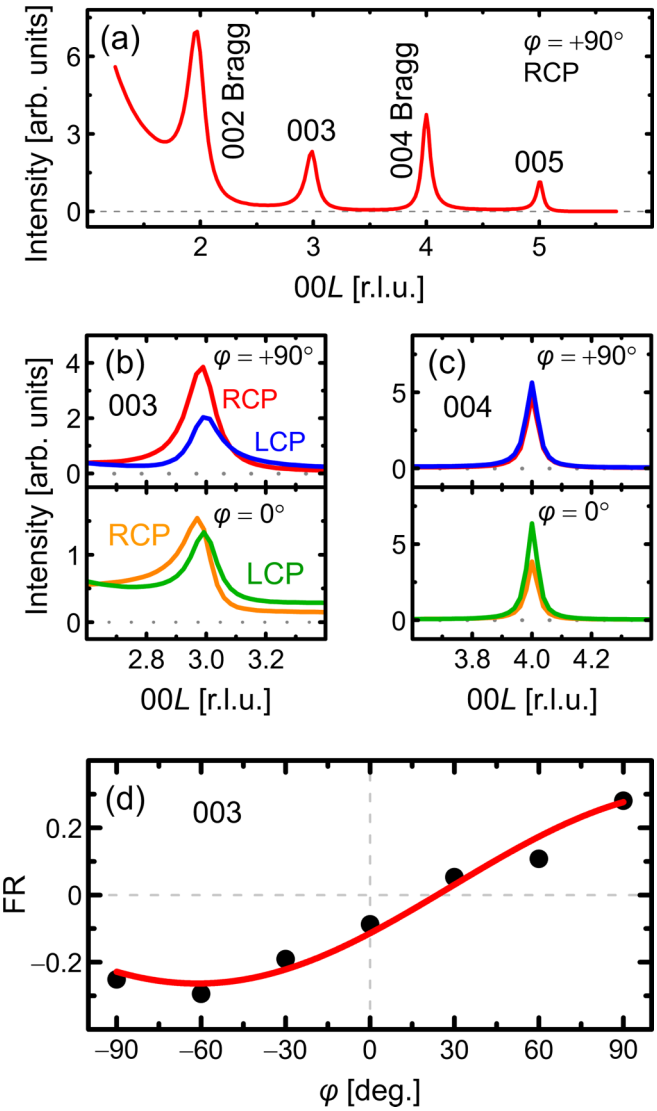

FIG. 3. (a)–(c) Resonant x-ray diffraction profiles of the 00L scan. Red and orange (blue and green) curves correspond to profiles obtained by RCP (LCP) x rays. The profile in the range from $L = 1.3$ to 5.7 (a). The profiles around $L = 3$ (b) and 4 (c). Here the profiles in (c) correspond to the data shown in Fig. 6(b). (d) Azimuthal-angle dependence of the flipping ratio (FR) at 003. A red curve is a fit to a sinusoidal function, $A\sin\varphi + B\cos\varphi + C$, where A, B, and C are constants. The gray dashed or dotted lines show the origin of each panel.

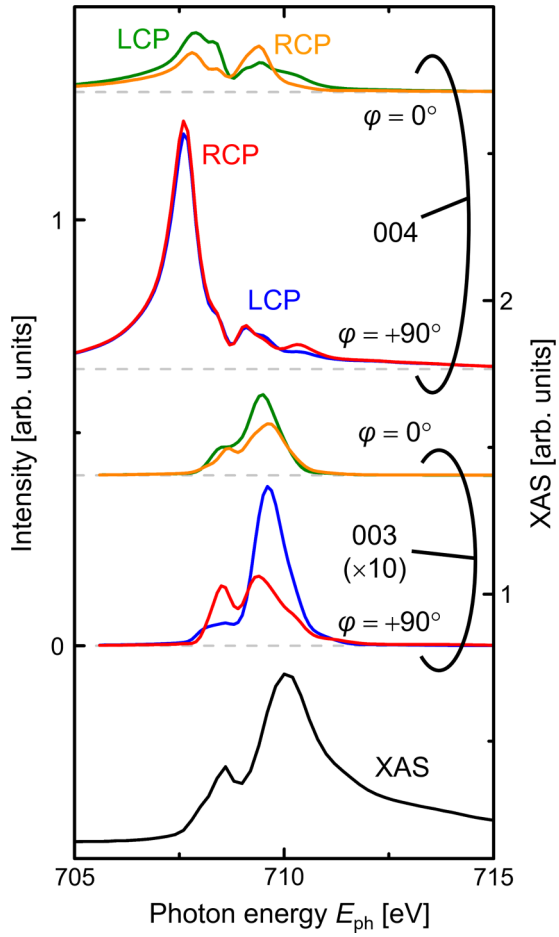

FIG. 4. Photon-energy profiles of 004 (upper) and 003 (middle) at the respective azimuthal angles and an XAS (bottom, a black line). Orange and red (green and blue) curves represent the data obtained by RCP (LCP) x rays. The gray dashed lines show the origin of each spectrum.

that the charge-magnetic interference effect represented by Eq. (8) is responsible for the circular dichroism of the 004 reflection. An M reversal in terms of the crystal axis [100], illustrated in Figs. 1(e) and 1(f), switches the sign of $(\frac{d\sigma}{d\Omega})^{004}_{P_2}$.

2. *Circular dichroism caused by the cycloidal spin-spiral order parameter*

In contrast to the circular dichroism of the 004 reflection, that of the 003 reflection is not trivial. Note that the cycloidal spin-spiral component with $\mathbf{k} = (0, 0, 1)$ contributes to the 003 reflection, but the collinear-ferrimagnetic one does not. In general, the intensity of magnetic satellites due to a cycloidal magnetic order can depend on the circularly polarized state of incident x rays through the pure magnetic scattering process represented in Eq. (5). The sign of $d\sigma/d\Omega_{P_2}$ corresponds to that of $\mathbf{C}$ in the cycloidal structure [36]. Applying the magnetic moments in Table I to Eq. (3), one gets $\mathbf{F}_m$ at 003 as

$$\mathbf{F}^{003}_m = 2N(\pm i m_L \sin\varphi \sin\beta,\ \mp i m_L \cos\varphi \sin\beta,\ m_S \sin\alpha). \tag{9}$$

TABLE I. The magnetic moments located at the respective blocks of the TC structure. Here φ is the azimuthal angle. The net magnetization, i.e., the cone axis, is set to be parallel to the scattering plane at $\varphi = 0°$ as illustrated in Fig. 2(b). m_S and m_L are the magnetic moments of an S block and an L block, respectively. α and β are the half opening angle of the conical structure in an S block and that in an L block, respectively. The positions of the moments in the unit cell along [001] are also shown, where $c \approx 52.07$ Å [16]. The upper and lower signs in the table correspond to the cycloidal spin-spiral domains shown in Figs. 1(g) and 1(h), respectively.

	Magnetic moment	Position
S1 block	$m_S \begin{pmatrix} -\cos\varphi\cos\alpha \\ -\sin\varphi\cos\alpha \\ \sin\alpha \end{pmatrix}$	0
L1 block	$m_L \begin{pmatrix} \cos\varphi\cos\beta \mp \sin\varphi\sin\beta \\ \sin\varphi\cos\beta \pm \cos\varphi\sin\beta \\ 0 \end{pmatrix}$	$c/4$
S2 block	$m_S \begin{pmatrix} -\cos\varphi\cos\alpha \\ -\sin\varphi\cos\alpha \\ -\sin\alpha \end{pmatrix}$	$c/2$
L2 block	$m_L \begin{pmatrix} \cos\varphi\cos\beta \pm \sin\varphi\sin\beta \\ \sin\varphi\cos\beta \mp \cos\varphi\sin\beta \\ 0 \end{pmatrix}$	$3c/4$

The double sign in Eq. (9) corresponds to the sign of $\mathbf{C}$ in the cycloidal component, i.e., right- and left-handed cycloidal spin-spiral domains [Figs. 1(g) and 1(h)]. When the cycloidal plane is parallel to the scattering plane, i.e., $\varphi = \pm 90°$ [Fig. 2(c)], Eqs. (5) and (9) indicate that no circular polarization dependence appears due to the orthogonal relation between $\mathbf{F}_m$ and $\widehat{\mathbf{q}'} \times \hat{\mathbf{q}}$. Thus, our experimental observation of the circular dichroism of 003 at $\varphi = +90°$ [see Fig. 3(b)] cannot be explained in terms of the pure magnetic scattering and suggests that the circular dichroism is ascribable to another origin.

A plausible origin of the circular dichroism at 003 is the charge-magnetic interference effect as in 004, because the interference can give rise circular dichroism on diffracted intensities even in antiferromagnets (e.g., the so-called alternating longitudinal conical structure of a Y-type hexaferrite [32]). Although the space group of Z-type hexaferrites has long been considered as $P6_3/mmc$, in which $002n \pm 1$ reflections are forbidden, finite $002n \pm 1$ reflections of Z-type $(Ba, Sr)_3Co_2Fe_{24}O_{41}$ with the TC structure were observed in recent nonresonant x-ray diffraction studies [24,37]. The experimental results indicate that the TC magnetic ordered phase somehow lowers the crystallographic symmetry of the Z-type hexaferrite. Therefore, the charge-magnetic interference is possibly finite and causes the circular dichroism at 003 which we observed in this experiment. Besides, the E_{ph} dependence of the scattering intensity of 003 is similar to that of the XAS (see Fig. 4). The similarity supports the presence of the interference effect, because the same factor $(F^1_{-1} + F^1_{+1})$ dominates both an XAS and an E_{ph} profile through the interference effect [32]. It is also worth noting that the asymmetric peak structure of the 003 reflection [see Fig. 3(b)] indicates the presence of the interference effect, which is

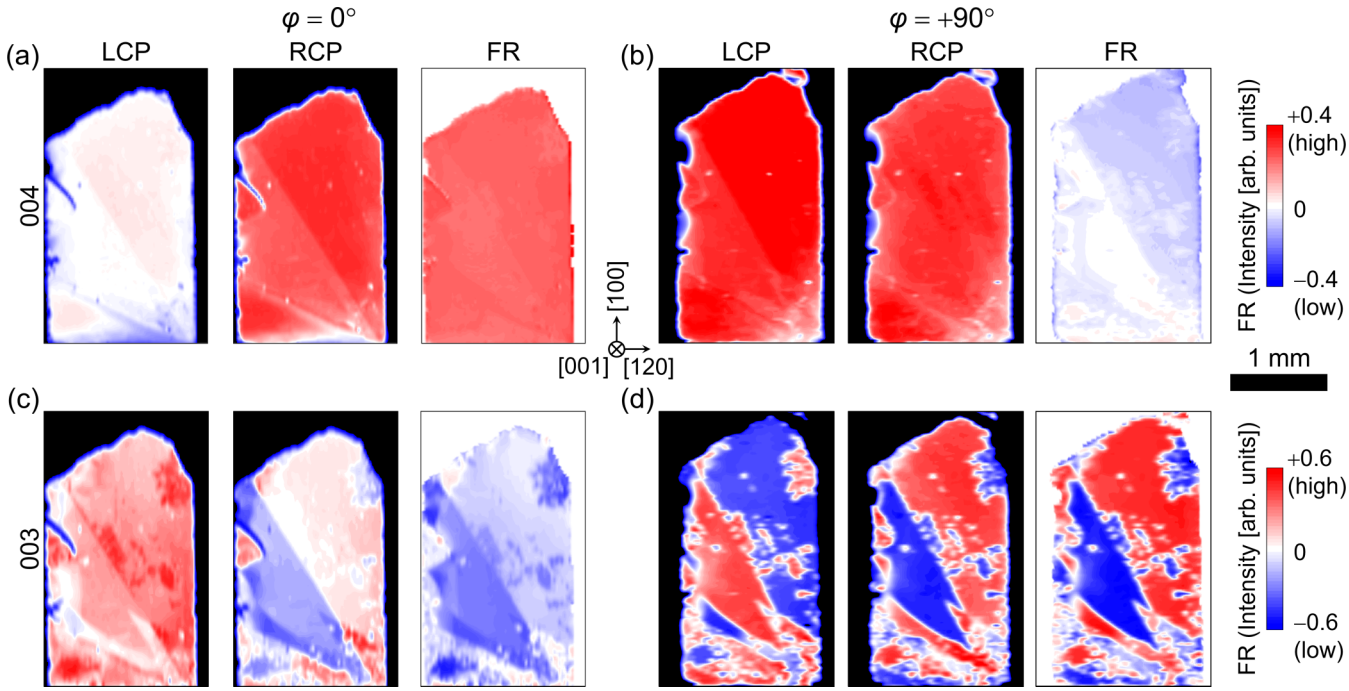

FIG. 5. Spatial distributions of scattering intensities by using LCP (left) and RCP (middle) x rays and flipping ratio (right) obtained at 004 (a), (b) and 003 (c), (d) in a magnetic field $B \approx 0.3$ T along [100]. Those in (a) and (c) [(b) and (d)] were taken at $\varphi = 0°$ [+90°]. The inhomogeneous patterns in the right panels of (c) and (d) show that right- and left-handed cycloidal spin-spiral domains coexist [Figs. 1(g) and 1(h)]. On the other hand, the homogeneous pattern in (a) shows that a single ferromagnetic domain is formed in the specimen.

probably in the form of crystal truncation rod scatterings [38,39].

In the presence of both the charge-magnetic interference and the pure magnetic scattering, $d\sigma/d\Omega_{P_2}$ at 003 is obtained as

$$\begin{aligned}\left(\frac{d\sigma}{d\Omega}\right)_{P_2}^{003} &= -P_2\mathrm{Im}\left(a_{003}{}^{*}b\mathbf{F}_m^{003}\right)\cdot(\hat{\mathbf{q}}+\hat{\mathbf{q}}'\cos 2\theta)\\ &\quad + P_2|b|^2\mathrm{Im}\left\{\left[\mathbf{F}_m^{003}\cdot(\hat{\mathbf{q}}'\times\hat{\mathbf{q}})\right]\left(\mathbf{F}_m^{003}\cdot\hat{\mathbf{q}}'\right)^{*}\right\}\\ &= \mp 4NP_2\mathrm{Re}(a_{003}{}^{*}b)m_L\sin\beta\cos^3\theta\sin\varphi\\ &\quad \mp 4N^2P_2|b|^2m_Lm_S\sin\alpha\sin\beta\sin\theta\sin 2\theta\cos\varphi\\ &\quad - 4NP_2\mathrm{Im}\left(a_{003}{}^{*}b\right)m_S\sin\alpha\sin^3\theta, \qquad (10)\end{aligned}$$

by using Eqs. (5) and (6). The double sign in Eq. (10) corresponds to the sign of **C** in the cycloidal component, i.e., right- and left-handed cycloidal spin-spiral domains [Figs. 1(g) and 1(h)]. Thus, the first and second terms in Eq. (10) show that the sign of **C** is detected through a circular dichroic signal. On the other hand, the last term in Eq. (10) is independent of the sign of **C** and gives an offset in FR. The first and third terms in Eq. (10) proportional to a^*b represent the charge-magnetic interference terms, while the second term corresponds to the pure magnetic scattering one. The first term in Eq. (10) shows that the circular dichroism can be present at $\varphi = \pm 90°$ due to the interference effect, even though the pure magnetic scattering (the second term) is absent. The circular dichroism observed experimentally at 003 matches up nicely with Eq. (10), including the FR, which shows a sinusoidal function of φ [Figs. 3(b) and 3(d)].

3. Observations of the two types of domains and their magnetic-field responses

Considering the discussions in the above two sections, one can capture the sign of the ferromagnetic order parameter and the cycloidal one by measuring the circular dichroism at 004 and 003, respectively. Furthermore, one can separately obtain domain structures formed by the respective order parameters by observing the spatial distribution of the circular dichroism at the corresponding reflections. Figure 5 shows the results of the intensity mapping measured at $B \approx 0.3$ T and room temperature for the 004 reflection (upper panels) and the 003 reflection (lower panels) of the crystal whose photo is shown in Fig. 2(a). The data were taken at both $\varphi = 0°$ [Figs. 5(a) and 5(c)] and $\varphi = +90°$ [Figs. 5(b) and 5(d)]. Note that the same color scale is used for the data obtained at the same reflection.

First, let us focus on the data taken by using 004 [see Figs. 5(a) and 5(b)]. The observed intensity profiles are nearly homogeneous in the whole sample region for both φ. (A weak intensity contrast between the right-upper and left-lower regions is ascribed to the crystallographic domains of which the crystal plane orientations are slightly different from each other. By taking FR, the effect of the crystallographic domains is eliminated because of the normalization and the information of magnetic domains is properly extracted.) The intensity at $\varphi = 0°$ strongly depends on the sign in P_2 of incident x rays while that at $\varphi = +90°$ is less affected, which is confirmed by the FR data [compare the right panels of Figs. 5(a) and 5(b)]. Such a circular polarization dependence is consistent with the results of the 00L scans [Fig. 3(c)] and E_{ph} profiles (Fig. 4). Because the sign of $d\sigma/d\Omega_{P_2}^{004}$ corresponds to the sign of M as

shown in Eq. (8), the homogeneous two-dimensional FR map indicates that a single ferromagnetic domain state is formed in the specimen at $B \approx 0.3$ T and room temperature.

In contrast to the results of 004 corresponding to the ferromagnetic domains, the two-dimensional 003 intensity profiles are inhomogeneous, as shown in Figs. 5(c) and 5(d). The FR map obtained at $\varphi = 0^\circ$ displayed in Fig. 5(c) shows a weak color contrast and has an offset to the negative direction. This is well explained by Eq. (10), where the finite second term represents the sign of **C**, i.e., cycloidal spin-spiral domains, and the third term provides an offset in FR while the first term is absent at $\varphi = 0^\circ$. Thus, the inhomogeneous pattern in the FR map is ascribed to the cycloidal spin-spiral domains, despite the presence of the offset. Quite similar but clearer inhomogeneous patterns are observed at $\varphi = +90^\circ$ [see Fig. 5(d)], where the finite first term in Eq. (10) represents the sign of **C** and the second term is absent. The clearer color contrast in Fig. 5(d) than that in Fig. 5(c) suggests that the magnitude of the charge-magnetic interference term is larger than that of the pure magnetic scattering term. This is consistent with the FR as a function of φ, as shown in Fig. 3(d). These results show that both the ferromagnetic domains and the cycloidal spin-spiral ones can be examined by taking FR maps of 004 and 003, respectively, through the dichroic interference effect.

The results of the resonant x-ray microdiffraction shown above indicate that this technique is applicable to the direct observation of the coupling between the ferromagnetic and the cycloidal spiral domains (or order parameters) in $Sr_3Co_2Fe_{24}O_{41}$. In order to observe how the reversal of B affects the magnetic domains, the intensity maps were obtained at 003 and 004. Figure 6 shows the respective magnetic domain structures. The most intense color contrast is observed at $\varphi = 0^\circ$ for 004 and at $\varphi = +90^\circ$ for 003. The domain states before B reversal are single-ferromagnetic and multicycloidal ones, as seen in the FR maps shown in Figs. 6(a) and 6(c), respectively. After B is reversed, the ferromagnetic domain is completely reversed [compare Figs. 6(a) and 6(b)]. In addition, the cycloidal spin-spiral domain pattern is perfectly intact but is reversed in its contrast by the B reversal [compare Figs. 6(c) and 6(d)]. The simultaneous inversion of the two types of domains by B reversal means that a reversal of M always accompanies that of **C** in the cycloidal component. This observation directly reveals the process of M reversal in the TC phase, that is, a 180° rotation of the cone axis around [001], which, for example, connects the structure shown in Fig. 1(c) to that in Fig. 1(d) or vice versa.

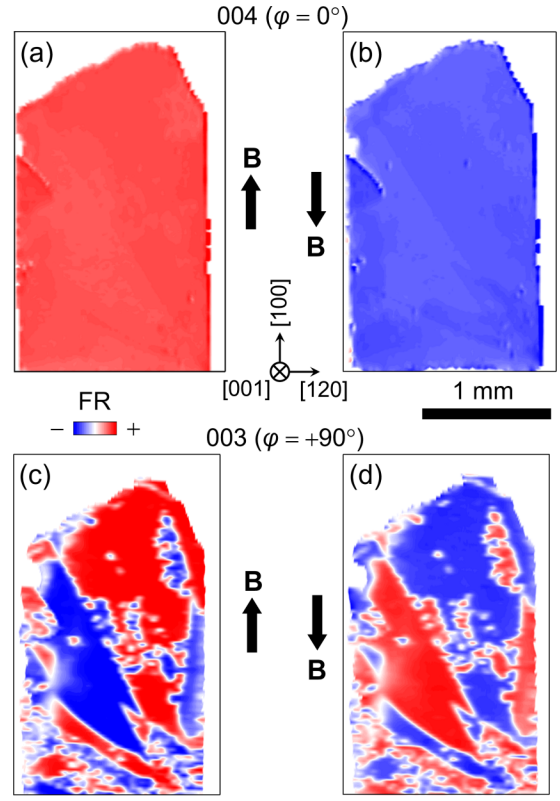

FIG. 6. The magnetic-field-reversal effect on domain structures. Spatial distributions of flipping ratio obtained at 004 (a), (b) and 003 (c), (d) in a magnetic field B represented by a black arrow. Those in (a) and (c) [(b) and (d)] were obtained before [after] a reversal of B. Red and blue regions in (a) and (b) correspond to ferromagnetic domains [Figs. 1(e) and 1(f)] while those in (c) and (d) correspond to cycloidal spin-spiral domains [Figs. 1(g) and 1(h)].

B. Magnetoelectric effect

Both the M-reversal process revealed in the previous section and the result of the B response of P, i.e., direct ME effect, lead us to understand the microscopic mechanism of the ME coupling in the Z-type hexaferrite. First, let us assume the spin-current (or inverse DM) mechanism ascribed to the asymmetric spin-exchange interaction [20–22]. The direction of P induced by this mechanism is reversed by the sign change in **C**. Therefore, if the ME coupling in the Z-type hexaferrite were ascribed to the spin-current mechanism alone, a reversal of M accompanying that of **C**, which was revealed by the present RXD study, should cause a perfect reversal of P. However, Ref. [16] reported that the sign of P induced by B is not changed by reversing that of B (or M), meaning that the spin-current mechanism cannot be a main origin of the ME coupling in the Z-type hexaferrite.

As a possible ME-coupling mechanism in the Z-type hexaferrite, the spin-dependent metal-ligand d-p hybridization mechanism [25] has been recently proposed [23,24]. In terms of the symmetry of the Z-type structure, an S block has inversion centers at its center plane while an L block has a mirror plane at its center [see Fig. 1(b)]. The local structural symmetries allow the in-plane component of P to be finite only in an L block but not in an S block. In the proposed magnetic structure [Fig. 1(c)], the in-plane component of the magnetic moments in an L block is coupled with that in an adjacent L block with a finite angle ($= 2\beta$). This spin configuration alone breaks the inversion symmetry lying in S blocks. Then macroscopic P is allowed along the basal plane.

To evaluate the contribution of the aforementioned two mechanisms to P, we calculated P through the spin-dependent metal-ligand d-p hybridization ($P_{d\text{-}p}$) and the asymmetric spin-exchange interaction (P_{asym}) as a function of magnetized direction represented by an angle Ψ. Ψ, termed magnetization angle, is defined as the angle between [100] and M as

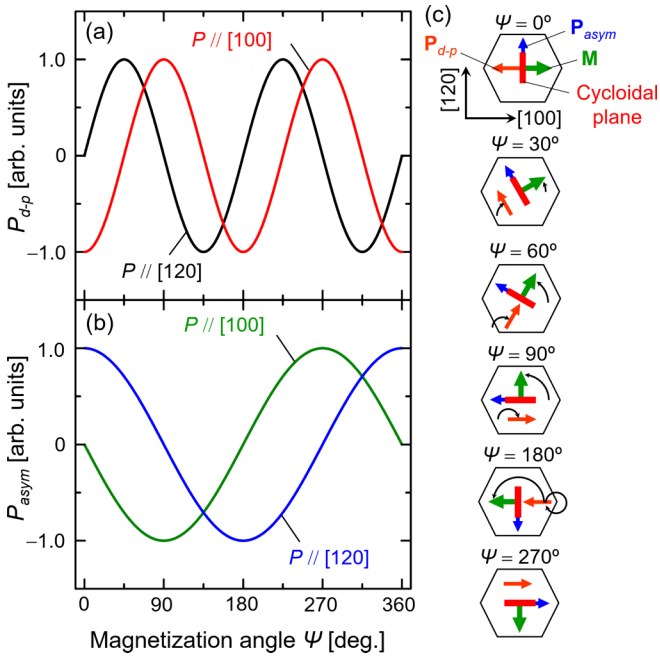

FIG. 7. The calculated results of magnetization angle Ψ dependence of electric polarization P along [100] and [120] originating from (a) the spin-dependent metal-ligand orbital hybridization and (b) the asymmetric spin-exchange interaction in the Z-type hexaferrite with the TC structure. These data were calculated by using the upper sign of magnetic moments shown in Table I. (c) The relation between $P_{d\text{-}p}$ (orange arrow) and $P_{\rm asym}$ (blue arrow) in terms of magnetization M (green arrow) normal to the cycloidal plane (red line) for several magnetization angles Ψ. Here magnetization angle Ψ is defined as the angle between [100] and M in the basal plane as illustrated in (c).

illustrated in Fig. 7(c). For the calculation, we employed the model structure where the magnetic moments of the respective magnetic sites within a magnetic block are placed parallel or antiparallel to the net magnetic moment represented in Table I with taking the magnetic interaction into account [26]. The local electric polarization p for each mechanism is obtained by using

$$\mathbf{p}_{d\text{-}p} = \hat{\mathbf{e}}_{il}(\hat{\mathbf{e}}_{il} \cdot \mathbf{m}_i)^2 \tag{11}$$

$$\mathbf{p}_{\rm asym} = \hat{\mathbf{e}}_{ij} \times (\mathbf{m}_i \times \mathbf{m}_j) \tag{12}$$

[20–22,25], respectively, where $\hat{\mathbf{e}}_{ij}$ is the unit vector of a bond vector between sites i and j. Equation (11) means p through the d-p hybridization between a magnetic site i and a surrounding ligand site l, while Eq. (12) means p through the asymmetric spin-exchange interaction between adjacent magnetic sites i and j. The sum of p through a crystal gives macroscopic electric polarization through the two mechanisms, $P_{d\text{-}p}$ and $P_{\rm asym}$. The results displayed in Fig. 7 show that the periodicities of $P_{d\text{-}p}$ and $P_{\rm asym}$ as a function of Ψ are 180° and 360°, respectively [see Figs. 7(a) and 7(b)]. The result of $P_{d\text{-}p}$ well agrees with the previous experimental data [23]. On the basis of the result of our calculations, we depict the geometrical relation among M, the cycloidal plane, $P_{d\text{-}p}$, and $P_{\rm asym}$ at several angles in Fig. 7(c). Our RXD study revealed that **C** is reversed by an M reversal, while the ME study showed that P is not reversed by an M reversal. To explain these experimental results consistently, $P_{d\text{-}p}$ should dominate the ME coupling in the Z-type hexaferrite [compare the illustrations at $\Psi = 0°$ and 180° (or $\Psi = 90°$ and 270°) in Fig. 7(c)].

To qualitatively estimate the contribution of $P_{d\text{-}p}$ to the ME coupling, we carried out ME measurements in several configurations, as illustrated in Fig. 8(c), where the relation between $P_{d\text{-}p}$ and $P_{\rm asym}$ in terms of M is obtained from our calculation [see also Fig. 7(c)]. Experimental results are shown in Figs. 8(a) and 8(b) in which the states 1 ∼ 6 and the processes I∼IV correspond to those in Fig. 8(c). The dominance of $P_{d\text{-}p}$ over $P_{\rm asym}$ is confirmed as a larger magnitude of P shown by an orange curve in Fig. 8(a) (process III) than that by a blue curve in Fig. 8(b) (process IV). Here the former reflects only $P_{d\text{-}p}$ [see states 1 and 3 in Fig. 8(c)] while the latter reflects only $P_{\rm asym}$ [see states 5 and 6 in Fig. 8(c)]. The 180° periodicity of $P_{d\text{-}p}$ as a function of Ψ is confirmed as a sign reversal of P by a 90° rotation of M (process II). $P_{d\text{-}p}$ and $P_{\rm asym}$ can be parallel or antiparallel depending on the orientation of M, and the observed P is the sum of them. The P in states 1 and 2 corresponds to $P_{d\text{-}p} + P_{\rm asym}$ and $P_{d\text{-}p} - P_{\rm asym}$, respectively [see the second top panel of Fig. 8(c)]. No sign change in P between states 1 and 2 [red curve in Fig. 8(a)] also confirms the dominance of $P_{d\text{-}p}$. Thus, we conclude that the nearly symmetric ME effect at an M reversal [red curve in Fig. 8(a) (process I)] is compatible with the **C** reversal, which was verified by the present RXD study, by employing the spin-dependent metal-ligand d-p hybridization as the main origin of the ME coupling in the Z-type hexaferrite.

C. Coupled order parameters based on the symmetry analysis

To comprehensively discuss the results of the RXD and ME-effect studies in terms of coupled order parameters based on the symmetry analysis, we introduce the following parameters: $M_{\langle 100\rangle}$, $M_{\langle 120\rangle}$, $P_{\langle 100\rangle}$, $P_{\langle 120\rangle}$, $C_{\{100\}}$, $C_{\{120\}}$, $C_{L1,L2}$, and T, characterizing the TC structure in the Z-type hexaferrite. Here $M_{\langle 100\rangle}$ and $P_{\langle 100\rangle}$ ($M_{\langle 120\rangle}$ and $P_{\langle 120\rangle}$) are M and P, respectively, along the equivalent directions of [100] ([120]), i.e., [100], [010], and $[\bar{1}\bar{1}0]$ ([120], $[\bar{2}\bar{1}0]$, and $[1\bar{2}0]$). Similarly, $C_{\{100\}}[C_{\{120\}}]$ is **C** in the cycloidal component whose cycloidal plane is in the equivalent planes of (100) [(120)], where $\mathbf{C}_{\langle 100\rangle} = C_{\langle 100\rangle}\hat{\mathbf{e}}_{[100]}$ and $\hat{\mathbf{e}}_{[100]}$ is the unit vector along [100]. $C_{L1,L2}$ is also **C** formed by a pair of adjacent magnetic moments in L blocks, L1 and L2, defined as $\mathbf{C}_{L1,L2} = C_{L1,L2}\hat{\mathbf{e}}_{[001]}$, and T is the toroidal moment defined as $\mathbf{T} = \mathbf{P} \times \mathbf{M} = T\hat{\mathbf{e}}_{[001]}$. These parameters are eigenvectors for the symmetry operations in the space group $P6_3/mmc$: (1) identity operation 1, (2) threefold rotational operation along [001] 3, (3) sixfold screw operation along [001] 6_3, (4) mirror operation normal to [100] $m_{(100)}$, (5) c glide operation normal to [120] c_g, (6) twofold rotational operation along [100] $2_{[100]}$, (7) that along [120] $2_{[120]}$, (8) inversion operation $\bar{1}$, (9) threefold rotoinversion operation $\bar{3}$, (10) sixfold rotoinversion operation $\bar{6}$, (11) mirror operation normal to [001] $m_{(001)}$, and (12) time-reversal operation t. Taking care of the location and orientation of the symmetry elements, one obtains the respective eigenvalues summarized in Table II.

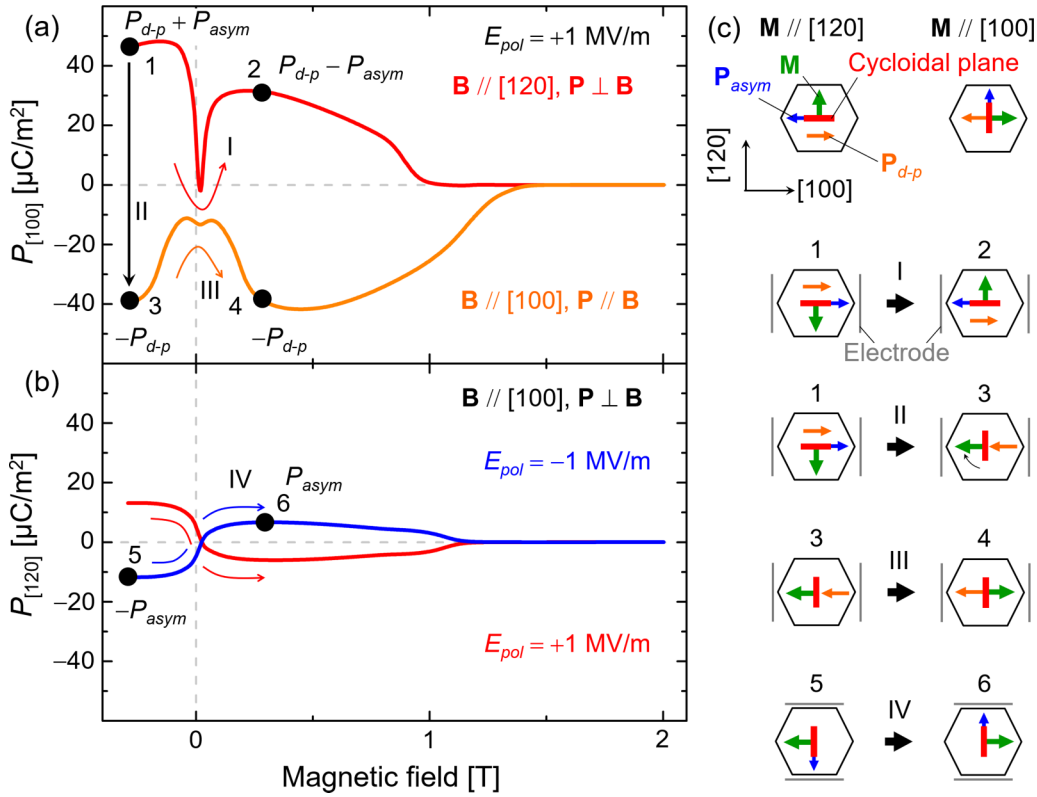

FIG. 8. Isothermal electric polarization along [100] (a) and [120] (b) as a function of a magnetic field B parallel to [100] or [120]. These data were obtained at 10 K. The Roman numbers show the processes in which B is reversed (I, III, and IV) or is rotated (II). (c) Illustrations of expected changes in the magnetic and electric configurations through the respective processes. The Arabic numbers denote the respective states labeled in (a) and (b). Red lines represent the cycloidal plane, and the directions of green, orange, and blue arrows indicate those of M, $P_{d\text{-}p}$, and P_{asym}, respectively.

Note that our symmetry analysis is to reveal what coupled order parameters are present in the free energy but not to calculate the tensor components of electric polarization as performed in Ref. [23].

A term in the free energy must be invariant for any symmetry operations in the higher symmetry phase. In other words, such a term belongs to the totally symmetric representation [6,40]. The symmetry analysis provides invariant terms in the TC phase of the hexaferrite as

$$U_1 = c_1 C_{\{100\}} P_{\langle 120\rangle} = c_1 C_{\{100\}} P^{\text{asym}}_{\langle 120\rangle}, \tag{13}$$

$$U_2 = c_2 C_{\{120\}} P_{\langle 100\rangle} = c_2 C_{\{120\}} P^{\text{asym}}_{\langle 100\rangle}, \tag{14}$$

$$V = c_3 C_{\text{L1,L2}} P_{\langle 100\rangle} = c_3 C_{\text{L1,L2}} P^{d\text{-}p}_{\langle 100\rangle}, \tag{15}$$

$$W_1 = c_4 M_{\langle 100\rangle} P_{\langle 120\rangle} T = c_4 M_{\langle 100\rangle} P^{\text{asym}}_{\langle 120\rangle} T^{\text{asym}}, \tag{16}$$

$$W_2 = c_5 M_{\langle 120\rangle} P_{\langle 100\rangle} T = c_5 M_{\langle 120\rangle} P^{\text{asym}}_{\langle 100\rangle} T^{\text{asym}}, \tag{17}$$

where $c_1 \sim c_5$ are coefficients for the respective terms. U_1, U_2, and V are trilinear coupling terms, because **C** is defined by two magnetic moments while W_1 and W_2 are fourth-order

TABLE II. Eigenvalues of the parameters characterizing the TC structure of the Z-type hexaferrite for symmetry operations in the space group $P6_3/mmc$ and irreproducible representations of the respective parameters.

	Eigenvalue												
Eigenvector	1	3	6_3	$m_{(100)}$	c_g	$2_{[100]}$	$2_{[120]}$	$\bar{1}$	$\bar{3}$	$m_{(001)}$	$\bar{6}$	t	Irreproducible representation
$M_{\langle 100\rangle}$	1	1	−1	1	−1	1	−1	1	1	−1	−1	−1	B_{1g}
$M_{\langle 120\rangle}$	1	1	−1	−1	1	−1	1	1	1	−1	−1	−1	B_{2g}
$P_{\langle 100\rangle}$	1	1	−1	−1	1	1	−1	−1	−1	1	1	1	B_{1u}
$P_{\langle 120\rangle}$	1	1	−1	1	−1	−1	1	−1	−1	1	1	1	B_{2u}
$C_{\{100\}}$	1	1	−1	1	−1	−1	1	−1	−1	1	1	1	B_{2u}
$C_{\{120\}}$	1	1	−1	−1	1	1	−1	−1	−1	1	1	1	B_{1u}
$C_{L1,L2}$	1	1	−1	−1	1	1	−1	−1	−1	1	1	1	B_{1u}
T	1	1	1	1	1	−1	−1	−1	−1	−1	−1	−1	A_{2u}

coupling terms. Higher-order terms as well as trivial second-order terms such as M^2 are ignored. Before going into detail, we remark that the origin of P is specified in the respective terms so as to make them surely invariant by adding affixes to P in Eqs. (13)–(17). This is because the characters of two P components ($P_{d\text{-}p}$ and P_{asym}) are different with respect to the 180° rotation of the TC structure around [001]. This rotation operation caused by an M reversal is not identical with any symmetry operations of $P6_3/mmc$. It is distinct from the previous discussions about coupled order parameters in spin-spiral-induced ferroelectrics possessing only the P_{asym} component [6,8,40–42]. In the case of M parallel to $\langle 100\rangle$, the directions of $P_{d\text{-}p}$ and P_{asym} are normal to each other. By contrast, in the case of M parallel to $\langle 120\rangle$, they are aligned along $\langle 100\rangle$, and the magnitude of $P_{\langle 100\rangle}$ is changed by the M reversal as discussed in Sec. III B. Then U_2, V, and W_2 including $P_{\langle 100\rangle}(= P_{d\text{-}p} + P_{\text{asym}})$ are no longer invariant for the M reversal. Thus, we need to identify $P_{\langle 100\rangle}$ and $P_{\langle 120\rangle}$ in the invariant terms as $P_{d\text{-}p}$ or P_{asym}. Taking into account this issue, let us go into the details of these equations. U_1 and U_2 show the coupling between C and P normal to M regardless of the direction of M, meaning that P in these terms is ascribed only to P_{asym} and that these terms describe usual trilinear ME interactions [6,8,40–42]. V shows the coupling between the canted moments in adjacent L blocks breaking the inversion symmetry and P along [100], where the direction of M can be along [100] or [120], i.e., $P_{d\text{-}p}$ [see Fig. 8(c)]. W_1 and W_2 represent the coupling among M, P normal to M independent of the direction of M, i.e., P_{asym}, and T. T is defined by M and P_{asym} which is normal to M.

We discuss how the order parameters are transformed at the M reversal by using Eqs. (13)–(17). The microscopic order parameters, i.e., C, are transformed by a 180° rotation of the conical structure around [001] from ($C_{\{100\}}$, $C_{\{120\}}$, $C_{L1,L2}$) to ($-C_{\{100\}}$, $-C_{\{120\}}$, $C_{L1,L2}$). To retain U_1, U_2, and V invariant, P is transformed from ($P^{\text{asym}}_{\langle 120\rangle}$, $P^{\text{asym}}_{\langle 100\rangle}$, $P^{d\text{-}p}_{\langle 100\rangle}$) to ($-P^{\text{asym}}_{\langle 120\rangle}$, $-P^{\text{asym}}_{\langle 100\rangle}$, $P^{d\text{-}p}_{\langle 100\rangle}$), as experimentally observed [see Fig. 8(c)]. As a result, the invariance of W_1, and W_2 preserves T as predicted previously in a conical magnet [3]. Therefore, the change in the microscopic order parameters revealed by the present RXD study well explains the changes in the macroscopic order parameters observed in the ME-effect study through the coupled order parameters allowed for the symmetry operations.

IV. CONCLUSION

In summary, we separately examined magnetic-field responses of two types of magnetic domains inherent in the transverse conical phase of a room-temperature multiferroic Z-type hexaferrite, $Sr_3Co_2Fe_{24}O_{41}$, by a resonant x-ray microdiffraction technique. A simultaneous inversion of the two components inherent in the transverse conical magnetic structure was observed for ferromagnetic domains and cycloidal spiral ones. On the basis of the observation, the magnetization-reversal mechanism in the transverse conical magnetic phase was clarified to be a 180° rotation of the cone axis about [001]. This magnetization-reversal mechanism, together with the characteristic magnetoelectric effects, leads us to the conclusion that the magnetoelectric coupling in the room-temperature multiferroic is mainly caused by the spin-dependent metal-ligand orbital hybridization with minor contribution from the asymmetric spin-exchange interaction. The change of order parameters by a magnetic field in the hexaferrite with the multielement ME couplings was described in terms of the coupled order parameters based on the symmetry analysis using the Landau theory. Our findings will contribute to the correct understanding of magnetoelectric couplings in multiferroics with complex crystallographic and magnetic structures.

ACKNOWLEDGMENTS

We thank H. Kawase for his help in sample preparation, and M. Soda, T. Asaka, M. Kenzelmann, and A. B. Harris for enlightening discussions. This work was supported by a Grant-in-Aid for JSPS Fellows (Grant No. JP16J02711) and KAKENHI Grants No. JP17H01143 and No. JP19H00661. Resonant x-ray diffraction experiments were performed at beamline 17SU at SPring-8 with the approval of RIKEN (Proposals No. 20170084 and No. 20180021).

[1] Y. Tokura, S. Seki, and N. Nagaosa, Multiferroics of spin origin, Rep. Prog. Phys. **77**, 076501 (2014).

[2] M. Fiebig, T. Lottermoser, D. Meier, and T. Morgan, The evolution of multiferroics, Nat. Rev. Mater. **1**, 16046 (2016).

[3] Y. Yamasaki, S. Miyasaka, Y. Kaneko, J.-P. He, T. Arima, and Y. Tokura, Magnetic Reversal of the Ferroelectric Polarization in a Multiferroic Spinel Oxide, Phys. Rev. Lett. **96**, 207204 (2006).

[4] J. S. White, T. Honda, K. Kimura, T. Kimura, Ch. Niedermayer, O. Zaharko, A. Poole, B. Roessli, and M. Kenzelmann, Coupling of Magnetic and Ferroelectric Hysteresis by a Multicomponent Magnetic Structure in Mn_2GeO_4, Phys. Rev. Lett. **108**, 077204 (2012).

[5] Y. Tokura, Multiferroics as quantum electromagnets, Science **312**, 1481 (2006).

[6] T. Honda, J. S. White, A. B. Harris, L. C. Chapon, A. Fennell, B. Roessli, O. Zaharko, Y. Murakami, M. Kenzelmann, and T. Kimura, Coupled multiferroic domain switching in the canted conical spin spiral system Mn_2GeO_4, Nat. Commun. **8**, 15457 (2017).

[7] N. Leo, V. Carolus, J. S. White, M. Kenzelmann, M. Hudl, P. Tolédano, T. Honda, T. Kimura, S. A. Ivanov, M. Weil, Th. Lottermoser, D. Meier, and M. Fiebig, Magnetoelectric inversion of domain patterns, Nature (London) **560**, 466 (2018).

[8] A. B. Harris, Identifying Landau order parameters and their transformation properties for complex multiferroics: The case of Mn_2GeO_4, Phys. Rev. B **96**, 054422 (2017).

[9] T. Kimura, Magnetoelectric hexaferrites, Annu. Rev. Condens. Matter Phys. **3**, 93 (2012).

[10] R. C. Pullar, Hexagonal ferrites: A review of the synthesis, properties and applications of hexaferrite ceramics, Prog. Mater. Sci. **57**, 1191 (2012).

[11] T. Kimura, G. Lawes, and A. P. Ramirez, Electric Polarization Rotation in a Hexaferrite with Long-Wavelength Magnetic Structures, Phys. Rev. Lett. **94**, 137201 (2005).

[12] S. Ishiwata, Y. Taguchi, H. Murakawa, Y. Onose, and Y. Tokura, Low-magnetic-field control of electric polarization vector in a helimagnet, Science **319**, 1643 (2008).

[13] V. Kocsis, T. Nakajima, M. Matsuda, A. Kikkawa, Y. Kaneko, J. Takashima, K. Kakurai, T. Arima, F. Kagawa, Y. Tokunaga, Y. Tokura, and Y. Taguchi, Magnetization-polarization cross-control near room temperature in hexaferrite single crystals, Nat. Commun. **10**, 1247 (2019).

[14] F. P. Chmiel, D. Prabahakaran, P. Steadman, J. Chen, R. Fan, R. D. Johnson, and P. G. Radaelli, Magnetoelectric domains and their switching mechanism in a Y-type hexaferrite, Phys. Rev. B **100**, 104411 (2019).

[15] Y. Tokunaga, Y. Kaneko, D. Okuyama, S. Ishiwata, T. Arima, S. Wakimoto, K. Kakurai, Y. Taguchi, and Y. Tokura, Multiferroic *M*-Type Hexaferrites with a Room-Temperature Conical State and Magnetically Controllable Spin Helicity, Phys. Rev. Lett. **105**, 257201 (2010).

[16] Y. Kitagawa, Y. Hiraoka, T. Honda, T. Ishikura, H. Nakamura, and T. Kimura, Low-field magnetoelectric effect at room temperature, Nat. Mater. **9**, 797 (2010).

[17] S. H. Chun, Y. S. Chai, B.-G. Jeon, H. J. Kim, Y. S. Oh, I. Kim, H. Kim, B. J. Jeon, S. Y. Haam, J.-Y. Park, S. H. Lee, J.-H. Chung, J.-H. Park, and K. H. Kim, Electric Field Control of Nonvolatile Four-State Magnetization at Room Temperature, Phys. Rev. Lett. **108**, 177201 (2012).

[18] S. Ishiwata, D. Okuyama, K. Kakurai, M. Nishi, Y. Taguchi, and Y. Tokura, Neutron diffraction studies on the multiferroic conical magnet $Ba_2Mg_2Fe_{12}O_{22}$, Phys. Rev. B **81**, 174418 (2010).

[19] M. Soda, T. Ishikura, H. Nakamura, Y. Wakabayashi, and T. Kimura, Magnetic Ordering in Relation to the Room-Temperature Magnetoelectric Effect of $Sr_3Co_2Fe_{24}O_{41}$, Phys. Rev. Lett. **106**, 087201 (2011).

[20] H. Katsura, N. Nagaosa, and A. V. Balatsky, Spin Current and Magnetoelectric Effect in Noncollinear Magnets, Phys. Rev. Lett. **95**, 057205 (2005).

[21] M. Mostovoy, Ferroelectricity in Spiral Magnets, Phys. Rev. Lett. **96**, 067601 (2006).

[22] I. A. Sergienko and E. Dagotto, Role of the Dzyaloshinskii-Moriya interaction in multiferroic perovskites, Phys. Rev. B **73**, 094434 (2006).

[23] Y. S. Chai, S. H. Chun, J. Z. Cong, and K. H. Kim, Magnetoelectricity in multiferroic hexaferrites as understood by crystal symmetry analyses, Phys. Rev. B **98**, 104416 (2018).

[24] S. H. Chun, K. W. Shin, K. H. Kim, J. F. Mitchell, P. J. Ryan, and J.-W. Kim, Microscopic observation of entangled multi-magnetoelectric coupling phenomenon, arXiv:1706.01144.

[25] T. Arima, Ferroelectricity induced by proper-screw type magnetic order, J. Phys. Soc. Jpn. **76**, 073702 (2007).

[26] J. Smit and H. P. J. Wijn, *Ferrites* (Philips' Technical Library, Eindhoven, 1959).

[27] Y. Takada, T. Nakagawa, M. Tokunaga, Y. Fukuta, T. Tanaka, and T. A. Yamamoto, Crystal and magnetic structures and their temperature dependence of Co_2 Z-type hexaferrite $(Ba, Sr)_3Co_2Fe_{24}O_{41}$ by high-temperature neutron diffraction, J. Appl. Phys. **100**, 043904 (2006).

[28] T. Takeuchi, A. Chainani, Y. Takata, Y. Tanaka, M. Oura, M. Tsubota, Y. Senba, H. Ohashi, T. Mochiku, K. Hirata, and S. Shin, An ultrahigh-vacuum apparatus for resonant diffraction experiments using soft x rays ($h\nu = 300$–$2,000$ eV), Rev. Sci. Instrum. **80**, 023905 (2009).

[29] Y. Hiraoka, Y. Tanaka, T. Kojima, Y. Takata, M. Oura, Y. Senba, H. Ohashi, Y. Wakabayashi, S. Shin, and T. Kimura, Spin-chiral domains in $Ba_{0.5}Sr_{1.5}Zn_2Fe_{12}O_{22}$ observed by scanning resonant x-ray microdiffraction, Phys. Rev. B **84**, 064418 (2011).

[30] L. D. Landau and E. M. Lifshitz, *Quantum Electrodynamics*, 2nd ed. (Pergamon Press, Oxford, 1982), Vol. 4.

[31] H. Nakajima, H. Kawase, K. Kurushima, A. Kotani, T. Kimura, and S. Mori, Observation of magnetic domain and bubble structures in magnetoelectric $Sr_3Co_2Fe_{24}O_{41}$, Phys. Rev. B **96**, 024431 (2017).

[32] H. Ueda, Y. Tanaka, Y. Wakabayashi, and T. Kimura, Observation of collinear antiferromagnetic domains making use of the circular dichroic charge-magnetic interference effect of resonant x-ray diffraction, Phys. Rev. B **98**, 134415 (2018).

[33] K. Namikawa, M. Ando, T. Nakajima, and H. Kawata, X-ray resonance magnetic scattering, J. Phys. Soc. Jpn. **54**, 4099 (1985).

[34] S. W. Lovesey and S. P. Collins, *X-Ray Scattering and Absorption by Magnetic Materials* (Oxford Science Publications, Clarendon Press, Oxford, 1996).

[35] N. Ishimatsu, H. Hashizume, S. Hamada, N. Hosoito, C. S. Nelson, C. T. Venkataraman, G. Srajer, and J. C. Lang, Magnetic structure of Fe/Gd multilayers determined by resonant x-ray magnetic scattering, Phys. Rev. B **60**, 9596 (1999).

[36] E. Schierle, V. Soltwisch, D. Schmitz, R. Feyerherm, A. Maljuk, F. Yokaichiya, D. N. Argyriou, and E. Weschke, Cycloidal Order of $4f$ Moments as a Probe of Chiral Domains in $DyMnO_3$, Phys. Rev. Lett. **105**, 167207 (2010).

[37] T. Asaka (private communication).

[38] G. M. Watson, D. Gibbs, G. H. Lander, B. D. Gaulin, L. E. Berman, H. Matzke, and W. Ellis, X-Ray Scattering Study of the Magnetic Structure Near the (001) Surface of UO_2, Phys. Rev. Lett. **77**, 751 (1996).

[39] G. M. Watson, D. Gibbs, G. H. Lander, B. D. Gaulin, L. E. Berman, H. Matzke, and W. Ellis, Resonant x-ray scattering studies of the magnetic structure near the surface of an antiferromagnet, Phys. Rev. B **61**, 8966 (2000).

[40] A. B. Harris, Landau analysis of the symmetry of the magnetic structure and magnetoelectric interaction in multiferroics, Phys. Rev. B **76**, 054447 (2007).

[41] G. Lawes, A. B. Harris, T. Kimura, N. Rogado, R. J. Cava, A. Aharony, O. Entin-Wohlman, T. Yildirim, M. Kenzelmann, C. Broholm, and A. P. Ramirez, Magnetically Driven Ferroelectric Order in $Ni_3V_2O_8$, Phys. Rev. Lett. **95**, 087205 (2005).

[42] M. Kenzelmann, A. B. Harris, S. Jonas, C. Broholm, J. Schefer, S. B. Kim, C. L. Zhang, S.-W. Cheong, O. P. Vajk, and J. W. Lynn, Magnetic Inversion Symmetry Breaking and Ferroelectricity in $TbMnO_3$, Phys. Rev. Lett. **95**, 087206 (2005).